ACS APPLIED MATERIALS & INTERFACES

Research Article

www.acsami.org

Mesoporous Hybrid Shells of Carbonized Polyaniline/Mn_2O_3 as Non-Precious Efficient Oxygen Reduction Reaction Catalyst

Shiyi Cao,[†] Na Han,[†] Jie Han,*[,†] Yimin Hu,[†] Lei Fan,[†] Chuanqiang Zhou,[‡] and Rong Guo*[,†]

[†]School of Chemistry and Chemical Engineering, Yangzhou University, Yangzhou, 225002, Jiangsu People's Republic of China

[‡]Testing Center, Yangzhou University, Yangzhou, Jiangsu 225009, People's Republic of China

Supporting Information

ABSTRACT: Mesoporous hybrid shells of carbonized polyaniline (C_{PANI})/Mn_2O_3 with well-controlled diameter and high surface area have been synthesized through surface protected calcination processes. Originating from polystyrene template, PANI, MnO_2, and SiO_2 were sequentially loaded, followed by template removal and calcination, resulting in the desired C_{PANI}/Mn_2O_3 hybrid shells. The introduction of SiO_2 shell was established to play the determining role in maintaining the configuration during calcination process under high temperature. The C_{PANI}/Mn_2O_3 hybrid shells showed outstanding electrocatalytic activity toward oxygen reduction reaction (ORR), with the onset potential at +0.974 V (versus RHE), the specific current at 60.8 mA/mg, and an overall quasi 4-electron transfer, which are comparable to those of the benchmark Pt/C. The remarkable ORR performance was attributed to the high specific surface area, the surface oxidation state of Mn, and composition-codependent behavior.

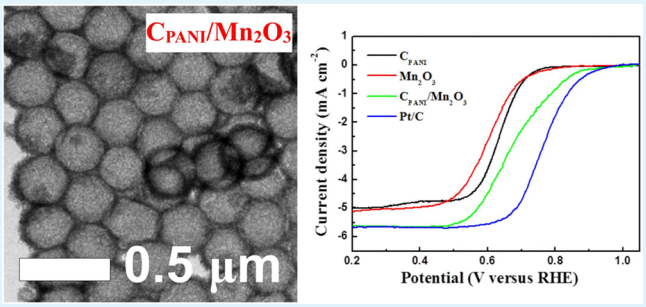

KEYWORDS: *oxygen reduction reaction, Mn_2O_3, carbonization, polyaniline, hollow spheres*

1. INTRODUCTION

Designed synthesis of high efficient catalysts for ORR has attracted considerable research attention because of their crucial role in electrochemical energy conversion and storage technologies.[1−4] The most studied ORR catalysts are Pt-based noble metals with superior overall catalytic performances.[5−7] Nevertheless, due to their high price and scarcity, exploiting efficient nonprecious catalysts is the research focus.[8−13] Transition metal oxides have been proved to be one of the most promising alternatives.[13−15] Among various transition metal oxides, manganese oxides (Mn_xO_y) have been extensively investigated due of their obvious advantages, such as abundance, low cost, and especially considerable catalytic activity toward ORR.[16−19]

Although showing insufficient stability in acidic media, Mn_xO_y can be used as a promising catalyst in air electrode for both alkaline fuel cells and metal-air batteries.[20,21] Recent studies have shown that the catalytic activity of Mn_xO_y toward ORR in alkaline media should be ascribed to the oxygen-containing groups and the redox reactions.[22−25] It has been shown that the catalytic performance of Mn_xO_y involved in ORR follows the sequence of Mn_5O_8 < Mn_3O_4 < Mn_2O_3 < MnOOH.[17,18] Formed at the various cathodes, Mn_2O_3 electrode is regarded to be the promising nonprecious electrocatalyst cathode.[26] However, due to their low conductivity and utilization, transition metal oxides show lower catalytic performances as compared to noble metal-based catalysts, leading to the limitation in practical applications.[27] Therefore, integrating conductive matrix in Mn_xO_y to enhance the electrocatalytic performance is significant. The most frequently used conductive matrix is carbon.[28−31] Recently, it has been revealed that N-doped carbon alone also shows catalytic activity toward ORR. In fact, such N-doped carbon as ORR catalyst has been first studied by Jasinski,[32] followed by Yeager and others.[33,34] Among various N-doped carbon, polyaniline (PANI) was selected as a intriguing template compound for N-doped carbon because of its favorable combination of aromatic rings and N-containing groups.[34] The heat treatment of PANI can realize the successful formation of N-doped carbon, and such N-doped carbon derived from carbonized PANI (C_{PANI}) has been proven to be efficient ORR catalyst.[35,36] Therefore, it is reasonable to believe that incorporation of PANI derived carbon within Mn_2O_3 will not only facilitate the electron transfer rate of Mn_2O_3, but also will contribute to the improved catalytic efficiency of the hybrids.

Herein, we reported the successful fabrication of mesoporous hybrid shells of C_{PANI}/Mn_2O_3 with well controlled diameter and high surface area through surface protected calcination processes. First, sulfonated polystyrene spheres (s-PS) were used as template, followed by chemical oxidation polymerization of aniline monomers to form s-PS/PANI core/shell hybrids. After the addition of $KMnO_4$ to s-PS/PANI core/shell colloidal solution, MnO_2 shells can be selectively formed on

Received: December 8, 2015
Accepted: February 16, 2016
Published: February 16, 2016

ACS Publications © 2016 American Chemical Society

DOI: 10.1021/acsami.5b11955
ACS Appl. Mater. Interfaces 2016, 8, 6040−6050

surfaces of PANI thanks to the redox activity between PANI and $KMnO_4$,[37,38] leading to the formation of s-PS/PANI/MnO_2 core/shell hybrids. After that, s-PS is removed and a thin silica shell is coated on surfaces of MnO_2 to form PANI/MnO_2/SiO_2 hybrid shells. The silica shell is critical to the formation of well-defined intact Mn_2O_3 shells during the calcination process. Finally, calcination treatment was employed to realize the crystalline transformation of manganese oxide from amorphous MnO_2 to crystalline Mn_2O_3 and carbonization of PANI, followed by removal of SiO_2 shells to obtain the resultant mesoporous C_{PANI}/Mn_2O_3 hybrid shells. Effects of SiO_2 shells, calcination temperature and atmosphere on resultant hybrid crystal form and morphology have been systematically investigated. The superior catalytic performance of C_{PANI}/Mn_2O_3 hybrid shells involved in ORR has been demonstrated, which suggests their intriguing potential as effective ORR nonprecious electrocatalysts.

2. EXPERIMENTAL METHODS

2.1. Materials. Aniline was distilled under reduced pressure before use. Tetraethyl orthosilicate (TEOS, 99.8%) was obtained from Sigma-Aldrich. $KMnO_4$ and other reagents (Sinopharm Chemical Reagent Co., Ltd., China) were of analytical grade and used without further purification. The water used in this study was deionized by milli-Q Plus system (Millipore, France), having 18.2 MΩ electrical resistivity.

2.2. Synthesis of s-PS Spheres. PS spheres (250 nm in diameter) were first prepared by emulsifier-free emulsion polymerization: Into a 250 mL three-necked flask, 28.0 mL of styrene and 150.0 mL of deionized water were added, and the solution was heated under mechanical stirring (400 rpm). When the temperature reached 95 °C, 0.1575 g of potassium peroxydisulfate was added. The polymerization was continued for 2 h under stirring. After that, the solvent was exchanged with ethanol by repeated centrifugation (11 000 rpm, 10 min) four times, and then the PS particles were isolated and dried at 60 °C for 12 h in an oven. The as-synthesized PS particles (0.40 g) were dispersed in deionized water under ultrasonication and then centrifuged to remove water. Then, 60 mL of concentrated sulfuric acid was added into the wet PS particles. The sulfonation reaction was allowed to proceed at 40 °C for 4 h under mechanical stirring (400 rpm). After that, the reaction solution was diluted with 60 mL of ethanol, and the supernatant was removed by centrifugation and washed with deionized water three times. Finally, s-PS particles were obtained by drying at 60 °C for 12 h in an oven.

2.3. Synthesis of s-PS/PANI Core/Shell Hybrids. s-PS particles (0.26 g) were dispersed in 30 mL of deionized water under sonication for 30 min. Subsequently, 0.06 mL of aniline in 4.0 mL of hydrochloric acid solution (2.0 mol L^{-1}) was added to the above s-PS colloidal solution and the solution was stirred at 0 °C for 2 h. Then ammonium persulfate (APS) dissolved in 5 mL deionized water (molar ration of APS to aniline is set at 1:1) was dropped into the colloidal solution. After that, the solution was centrifuged, and the precipitate was washed with deionized water and ethanol, and then dried at 60 °C for 12 h in an oven.

2.4. Synthesis of PANI/MnO_2 Hybrid Shells. The as-formed s-PS/PANI core/shell hybrids were dispersed in 10.0 mL deionized water, followed by the addition of hydrochloric acid (12.0 mL, 1.0 mol L^{-1}) and 150 mL deionized water, and then the solution was stirred for 30 min. After that, $KMnO_4$ aqueous solution (50 mL, 0.025 mol L^{-1}) was added in one portion, and the reaction was allowed to take place for 4 h. After that, the solution was centrifuged, and the precipitate was washed with deionized water and ethanol. Then 10.0 mL tetrahydrofuran (THF) was added to dissolve s-PS cores under stirring for 12 h. The solution was centrifuged, and the precipitate was washed with deionized water and ethanol three times and then dried at 60 °C for 12 h in an oven.

2.5. Synthesis of Mesoporous C_{PANI}/Mn_2O_3 Hybrid Shells. PANI/MnO_2 hollow spheres (0.05 g) were dispersed in mixed solution containing deionized water (4.25 mL) and ethanol (5 mL), and then the colloidal solution was stirred for 30 min. After that, 5 mL of ammonia and 100 μL of TEOS was added, and the reaction was allowed to take place for 3 h. After that, the solution was centrifuged, and the precipitate was washed with deionized water and ethanol. The as-synthesized PANI/MnO_2/SiO_2 hollow spheres were then dried at 60 °C for 12 h in an oven, and calcinated at a certain high temperature for 12 h under the protection of nitrogen atmosphere, realizing the crystalline transformation of manganese oxide from amorphous MnO_2 to crystalline Mn_2O_3 and carbonization of PANI. The obtained $C_{PANI}/Mn_2O_3/SiO_2$ hollow spheres were subjected to etch SiO_2 shells with sodium hydroxide (40 mL, 0.25 mol L^{-1}). The etching reaction was allowed to proceed at 70 °C for 6 h under stirring. After that, the solution was centrifuged, and the precipitate was washed with deionized water and ethanol, and then dried at 60 °C for 12 h in an oven for further use as catalysts.

2.6. Instruments. Morphologies were examined by a transmission electron microscopy (TEM, Tecnai-12 Philip Apparatus Co., United States) and a high resolution transmission electron microscopy (HR-TEM, Tecnai G2 F30 S-Twin TEM, FEI, Holland). Fourier transform infrared spectrometry (FTIR) spectra were recorded in the range of 400−4000 cm^{-1} using FTIR spectroscopy (Tensor 27, Bruker, Germany). The samples were prepared in a pellet form with spectroscopic grade KBr. X-ray diffraction (XRD) patterns were recorded on a German Bruker AXS D8 ADVANCE X-ray diffractometer. The products were recorded in the 2θ range from 10 to 80° in steps of 0.04° with a count time of 1 s each time. The specific surface area and pore size were studied by using a Beishide 3H-2000PS2 analysis instrument. The surface area was determined from the adsorption isotherm using the multipoint Brunauer−Emmett−Teller (BET) method in the pressure P/P_0 range of 0.04−0.32. The desorption isotherm were used to determine the average pore size and distribution by the Barrett−Joyner−Halenda (BJH) method. X-ray photoelectron spectroscopy (XPS) data were recorded on a Thermo ESCALAB 250 using a nonmonochromatized Al Kα X-ray (1486.6 eV) as the excitation source and choosing C 1s as the reference line. The electrochemical impedance spectra (EIS) were performed on an electrochemical workstation (PGSTAT30, Auto Lab) by using three-electrode cells. The resultant electrode served as the working electrode, with a platinum wire as the counter electrode, and a saturated calomel electrode (SCE) as the reference electrode. The measurements were performed in 0.1 mol L^{-1} KOH solution.

2.7. Electrochemical Tests. Electrochemical tests were conducted using a standard three-compartment electrochemical cell. A Pt foil was used as the reference electrode and a saturated calomel electrode (SCE) was used as the counter electrode. The glass carbon (GC) substrate was coated with different catalysts and applied as the working electrode, which was confined in a rotating disk electrode (RDE, 5.61 mm in diameter) or a rotating ring-disk electrode (RRDE, Pt ring and GC disk, 6.25 mm in disk diameter). The working electrode was prepared as follows. At first, 3.0 mg catalyst mixed with 7.0 mg Cabot Vulcan XC-72 carbon (Vc-72) were transferred into a glass containers containing 950 μL of 2-propanol mixed with 950 μL of water and 50 μL of Nafion solution (5 wt %, Sigma-Aldrich). The suspension was ultrasonically dispersed to form a homogeneous ink. After that, 7 μL of the ink was pipetted onto the GC electrode and then was naturally drying for 4 h to form a thin catalyst layer on the GC electrode.

The tests were conducted on a computer-controlled potentionstat/galvanostat workstation at room temperature. The supporting electrolyte was 0.1 mol L^{-1} KOH aqueous solution, which was purged with Ar or O_2 (Air Product, purity 99.995%) for at least 30 min prior to testing and maintained under Ar or O_2 atmosphere during the test. Voltammograms were recorded from 0.2 to −0.8 V versus SCE under quasi-steady-state conditions (5 mV s^{-1}). The rotation speed was measured as round per minute (rpm). All potentials were reported with reference to the reversible hydrogen electrode (RHE) potential scale. In 0.1 mol L^{-1} KOH solution, the potential of SCE was calibrated as +0.990 V with respect to RHE.

DOI: 10.1021/acsami.5b11955
ACS Appl. Mater. Interfaces 2016, 8, 6040−6050

3. RESULTS AND DISCUSSION

3.1. C_{PANI}/Mn_2O_3 Hybrid Shells: Formation Mechanism, Morphology and Characterization. Scheme 1

Scheme 1. Schematic Illustration of the Procedures for the Synthesis of Mesoporous C_{PANI}/Mn_2O_3 Hybrid Shells

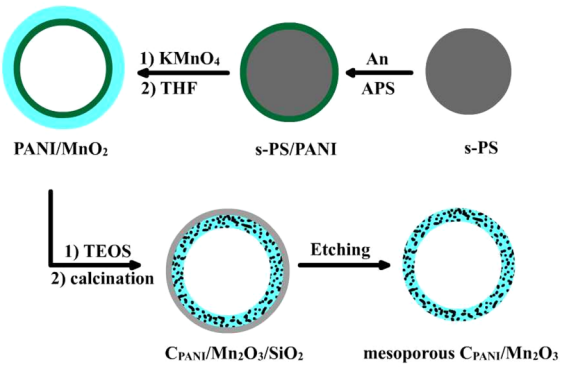

illustrates the general procedures for C_{PANI}/Mn_2O_3 hybrid shells. First, aniline monomers were added into s-PS colloidal solution and selectively adsorbed on s-PS surfaces through electrostatic interactions, followed by the chemical oxidation polymerization process after addition of oxidant to yield PANI shells on s-PS surfaces. After addition of $KMnO_4$ to s-PS/PANI core/shell colloidal solution, MnO_2 shells can be selectively formed on surfaces of PANI thanks to the redox activity between PANI and $KMnO_4$,[37,38] leading to the formation of s-PS/PANI/MnO_2 core/shell hybrids. After that, s-PS is selectively removed using THF solvent and a thin silica shell is coated on surfaces of MnO_2 to form PANI/MnO_2/SiO_2 hybrid shells by adapting the well-known Stöber method[39] using ethanol–water mixed solvent. Finally, calcination treatment was employed to realize the crystalline transformation of manganese oxide from amorphous MnO_2 to crystalline Mn_2O_3 and carbonization of PANI, followed by SiO_2 shells removal with the aid of NaOH solution to selective dissolve dense to obtain the resultant mesoporous C_{PANI}/Mn_2O_3 hybrid shells.

Figure 1a shows the TEM image of s-PS spheres with uniform size (250 nm in diameter) and smooth surfaces. Figure 1b shows the typical TEM images of s-PS/PANI core/shell hybrids. Rough surfaces indicate successful coating of PANI, where PANI shell thickness is measured to be 35 nm when s-PS cores are removed using THF solvent (inset in Figure 1b). After addition of $KMnO_4$ to s-PS/PANI colloidal solution, MnO_2 can be formed on PANI surfaces. We have previously reported that PANI can act as reactive template for the synthesis of PANI/MnO_2 hybrids when PANI encounter $KMnO_4$, where benzenoid rings in PANI are oxidized into quinonoid rings and Mn(VII) in $KMnO_4$ is reduced into Mn(IV).[37] It can be observed that the surfaces of PANI were covered by a thin layer of MnO_2 nanosheets (~20 nm) after the addition of $KMnO_4$ (Figure 1c). The removal of s-PS cores can be accomplished starting from s-PS/PANI or s-PS/PANI/MnO_2 core/shell hybrids, where the as-formed PANI/MnO_2 hollow hybrids show the same morphology. Finally, SiO_2 protecting shells were coated on surfaces of PANI/MnO_2 hollow hybrids. As outer surfaces of PANI/MnO_2 hybrid shells are rough, SiO_2 shown as interconnected nanospheres (~50 nm in diameter) rooted on MnO_2 surfaces (Figure 1d).

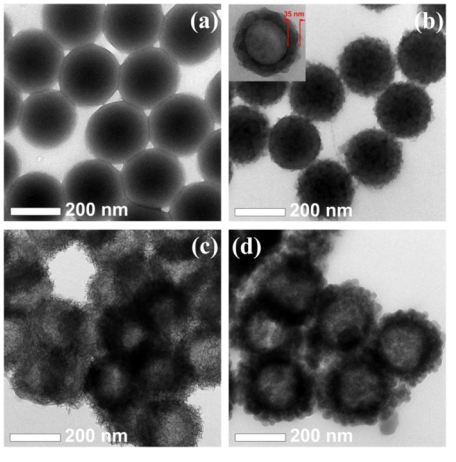

Figure 1. TEM images of (a) s-PS spheres, (b) s-PS/PANI core/shell hybrids, (c) PANI/MnO_2 hybrid shells, and (d) PANI/MnO_2/SiO_2 hybrid shells. Inset in panel b shows shell thickness of PANI after s-PS removal.

After calcination and etching processes, PANI/MnO_2/SiO_2 can be transformed into mesoporous C_{PANI}/Mn_2O_3 hybrid shells. Figure 2a represents the typical TEM image of mesoporous C_{PANI}/Mn_2O_3 hybrid shells with well-defined spherical morphology and narrow size distribution (300 nm in diameter). A magnified TEM image as shown in Figure 2b reveals the shell thickness of ca. 40 nm, which is thinner than that of PANI/MnO_2 hybrid shells (ca. 55 nm), suggesting volume shortage of hybrid shells during calcination process. Inset in Figure 2b depicts the HRTEM image of C_{PANI}/Mn_2O_3 hybrid shells, where the fringe spacing of 0.633 nm as observed proves anatase Mn_2O_3 (440) plane (JCPDS No. 41-1442). Furthermore, the energy dispersive X-ray spectroscopic (EDS) elemental maps of Mn (Figure 2c), O (Figure 2d), C (Figure 2e), and N (Figure 2f) further confirm the successful formation of C_{PANI}/Mn_2O_3 hybrid shells. It should be noted that PANI has been carbonized into nitrogen-containing carbon, and carbon is completely penetrated into MnO_2 porous shells during the calcination process.

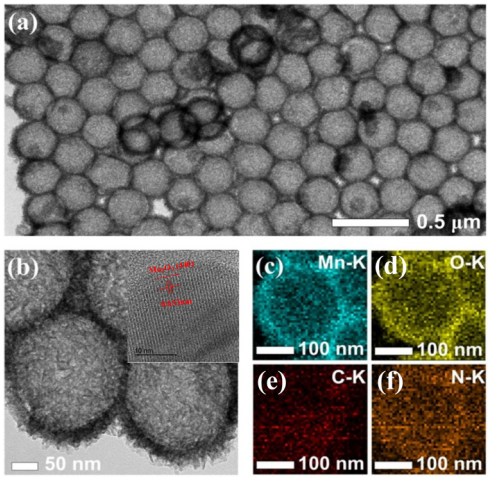

Figure 2. (a, b) TEM images and (c–f) EDS maps of Mn, O, C and N for mesoporous C_{PANI}/Mn_2O_3 hybrid shells derived from PANI/MnO_2/SiO_2 calcined at 800 °C under inert atmospheres after silica removal. Inset in panel b shows the HRTEM image of mesoporous C_{PANI}/Mn_2O_3 hybrid shells.

DOI: 10.1021/acsami.5b11955
ACS Appl. Mater. Interfaces 2016, 8, 6040–6050

It was found that the SiO_2 shells had the determining role in preserving the original hollow morphology under high temperature. In a control experiment, PANI/MnO_2 hybrid shells without SiO_2 coating were calcined under the same condition to PANI/MnO_2/SiO_2 (800 °C under inert atmosphere), and the resultant TEM is given in Figure 3a. It

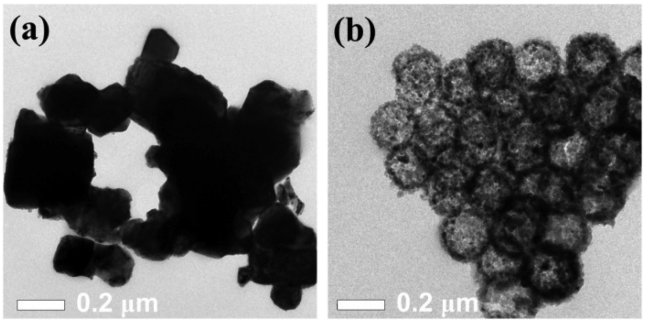

Figure 3. (a) TEM image of C_{PANI}/Mn_2O_3 hybrids derived from PANI/MnO_2 calcined at 800 °C under inert atmosphere. (b) TEM image of Mn_2O_3 hollow spheres derived from PANI/MnO_2/SiO_2 calcined at 800 °C under air after silica removal.

is seen that the original hollow structures have been completed destroyed, and only agglomerated solid particles can be verified. This is mainly due to the strain generated in the hollow structure with the increments in the crystallinity and crystallite size with the dominant Mn_2O_3 phase. As a result, it can be indicated that SiO_2 plays as the protecting shell in preserving the original hollow structure. In another control experiment, PANI/MnO_2/SiO_2 hybrid shells were calcined at 800 °C under air to completely removal of carbon. Figure 3b shows the typical TEM image of Mn_2O_3 hollow spheres after removal of SiO_2 shells. In comparison with C_{PANI}/Mn_2O_3 hollow spheres given in Figure 2, the shell thickness has decreased to 30 nm due to the carbon structure reduction (about 20 wt % as measured from energy-dispersive X-ray spectroscopy). In addition, obvious nanocavities can be observed in Mn_2O_3 shells, which are seldom seen in C_{PANI}/Mn_2O_3 hybrid shells. The results further confirm that carbon is completely penetrated into Mn_2O_3 porous shells of C_{PANI}/Mn_2O_3 hybrids.

The temperature-dependent sequential changes in morphology were also investigated. It is found that the resultant morphology is comparable to Figure 2 when the calcination temperature is below 800 °C. For instance, C_{PANI}/MnO_2 hybrid shells as calcined at 560 °C (Figure 4a) show similar morphology and size to Figure 2 as calcined at 800 °C. If the temperature increased to 900 °C, Mn_2O_3 nanocrystals with size about 30 nm could be clearly seen, and the morphology could be preserved in the presence of SiO_2 shells (Figure 4b). After removal of SiO_2 shells, the hollow structures collapse as shown in Figure 4c. The C_{PANI}/Mn_2O_3 hybrid shells with discrete large Mn_2O_3 nanocrystals show decreased strength in supporting the hollow morphology after removal of SiO_2 shells. When the calcination temperature further increase to 1000 °C, the original structures merged into each other and collapsed before the SiO_2 removal process (Figure 4d). Thus, it can be indicated that SiO_2 plays as the protecting shell in preserving the original hollow structure when the calcination temperature is below 900 °C. However, with the temperature rising, the protective layer of silica cannot play a protective role anymore.

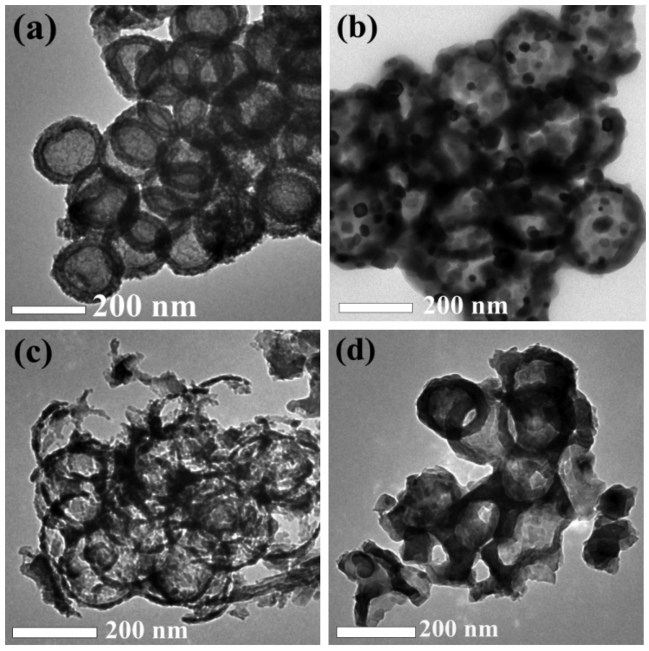

Figure 4. (a) TEM image of C_{PANI}/MnO_2 hybrid shells derived from PANI/MnO_2/SiO_2 hybrid shells calcined at 560 °C under inert atmosphere. (b) TEM image of $C_{PANI}/Mn_2O_3/SiO_2$ hybrid shells derived from PANI/MnO_2/SiO_2 hybrid shells calcined at 900 °C under inert atmosphere. (c) TEM image of carbon/Mn_2O_3 hybrid shells derived from PANI/MnO_2/SiO_2 hybrid shells calcined at 900 °C under inert atmospheres after silica removal. (d) TEM image of $C_{PANI}/Mn_2O_3/SiO_2$ hybrid shells derived from PANI/MnO_2/SiO_2 hybrid shells calcined at 1000 °C under inert atmosphere.

XRD patterns were used to determine the phase structures of as-formed hybrids. As observed in Figure 5a, the original PANI/MnO_2 hybrid shells before calcination (Figure 1c) only shows a broad band that corresponds to amorphous PANI,[40] and the typical peaks for MnO_2 is not shown, suggesting the amorphous features of MnO_2. At the calcination temperature of 560 °C (Figure 4a), $C_{PANI}/MnO_2/SiO_2$ hybrid shells show no typical peaks for manganese oxides (Figure S2a). However, when the silica of $C_{PANI}/MnO_2/SiO_2$ hybrid shells is removed, the typical peaks for MnO_2 can be clearly seen. As for PANI/MnO_2/SiO_2 hybrid shells calcined at 800 °C under inert atmospheres after silica removal (Figure 2), all the diffraction peaks can be assigned to Mn_2O_3 (JCPDS No. 71−0636). At the calcination temperature of 900 °C, sharper diffraction peaks (Figure S1) indicate better crystallinity, which is consistent with morphology observations.

Figure S2a gives the FTIR spectra of PANI/MnO_2 and C_{PANI}/MnO_2 hybrid shells. As for PANI/MnO_2, the characteristic peaks for PANI can be found, such as the stretching vibration of quinonoid rings (1609 cm^{-1}) and benzenoid rings (1494 cm^{-1}), the aromatic C−H in-plane bending modes (1172 cm^{-1}), out-of-plane deformations of C−H bonds on 1,4-disubstituted rings (756 cm^{-1}).[41−43] The 2500−4000 cm^{-1} part of the spectrum reflects especially hydrogen bonding. The strong absorption appearing at wavenumber 537 cm^{-1} can be ascribed to the characteristic Mn−O stretching vibration in manganese oxides. In the case of C_{PANI}/MnO_2, the characteristic peaks for PANI are no more observable, reflecting dehydrogenation of PANI during carbonization and the formation of fused-ring structures.[44] In addition, the stretching vibration of Mn−O bond remains and has been strengthened,

DOI: 10.1021/acsami.5b11955
ACS Appl. Mater. Interfaces 2016, 8, 6040−6050

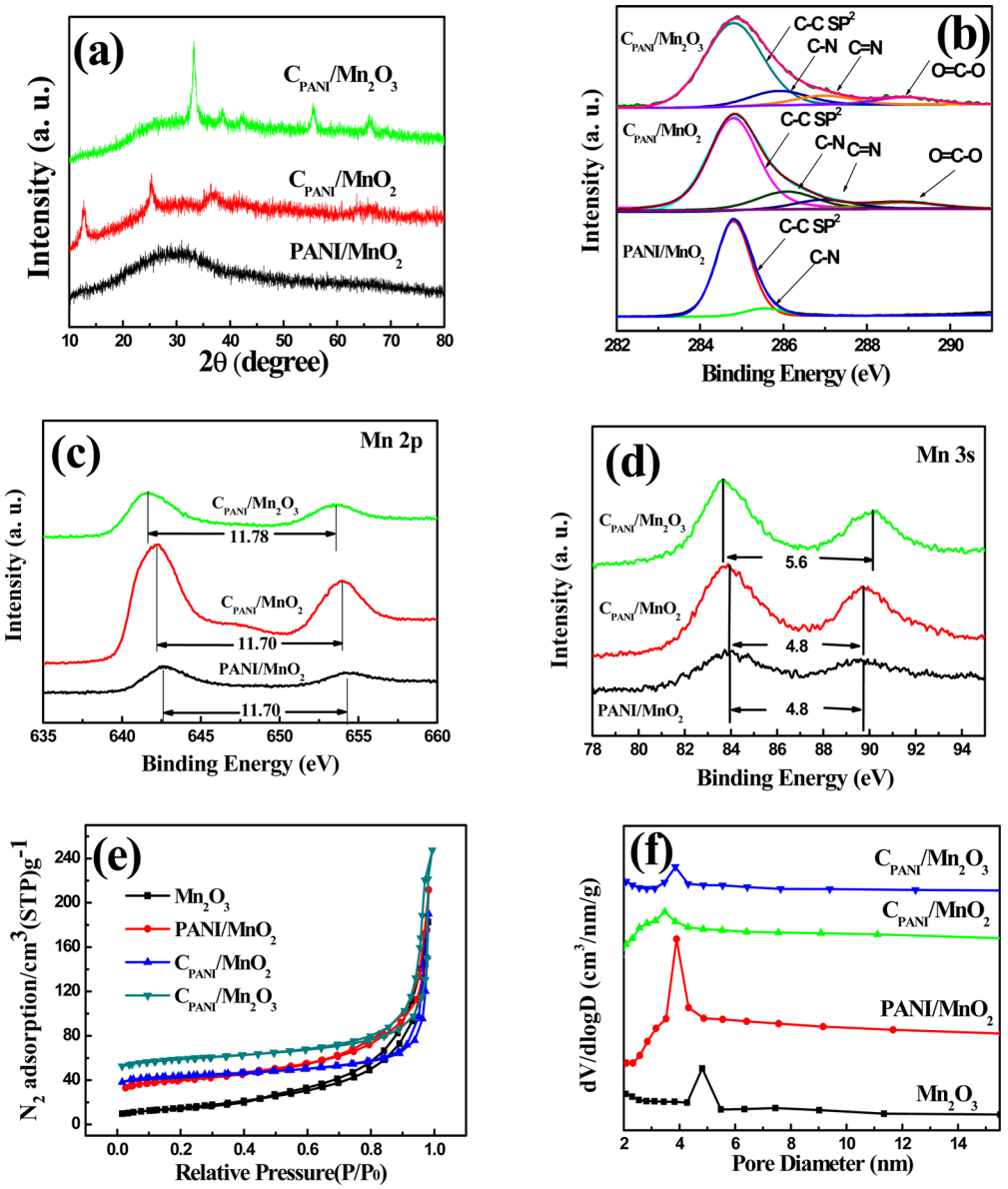

Figure 5. (a) XRD and (b-d) XPS spectra of PANI/MnO_2, C_{PANI}/MnO_2 and C_{PANI}/Mn_2O_3 hybrid shells derived from PANI/MnO_2/SiO_2 calcined at different temperature under inert atmospheres after silica removal, (e) N_2 adsorption−desorption isotherms of Mn_2O_3, PANI/MnO_2, C_{PANI}/MnO_2 and C_{PANI}/Mn_2O_3 hybrid shells hybrid shells and (f) their corresponding pore size distribution.

confirming the presence of manganese oxide. The carbonization of PANI has been further confirmed from Roman spectrum (Figure S2b), where the two bands centered at 1589 cm^{-1} (G band) and 1345 cm^{-1} (D band) indicating the formation of disordered graphite.[44,45]

XPS technique has been utilized to further confirm the composition and chemical nature of PANI/MnO_2, C_{PANI}/MnO_2, and C_{PANI}/Mn_2O_3 hybrid shells. The signatures of C, O, and Mn for PANI/MnO_2, C_{PANI}/MnO_2, and C_{PANI}/MnO_2 hybrid shells (Figure S3) have been confirmed. Additional signature for Si as observed in C_{PANI}/MnO_2 and C_{PANI}/Mn_2O_3 hybrid shells should come from SiO_2 residual after SiO_2 etching process. Deconvolution is employed to resolve the contribution of different types of carbon. The peaks at 284.8, 285.9, 287.0, and 288.9 eV (Figure 5b) are ascribed to the binding energy of sp^2 C−C, C−N, C═N, and O═C−O bonds, respectively.[46] The C 1s spectrum of PANI/MnO_2 shows peaks at 284.8 (C−C) and 285.9 eV (C−N). As for the C 1s spectra of C_{PANI}/MnO_2 and C_{PANI}/Mn_2O_3, in addition to one main peak centered at 284.8 eV (C−C) and 285.9 eV (C−N), peaks centered at 287.0 (C═N) and 288.9 eV (O═C−O) are also appeared. The increased relative intensity of C−N peak and the appearance of C═N peak proves carbonization of PANI at high temperature. It can be explained that cross-linked PANI with phenazine units have been produced.[47] Moreover, the PANI cross-links with manganese oxides in the carbonization process of PANI, which explains the emergence of O═C−O peak.

The high resolution Mn 2p spectra for PANI/MnO_2 C_{PANI}/MnO_2 and C_{PANI}/Mn_2O_3 are presented in Figure 5c. The peaks of PANI/MnO_2 centered at 642.85 and 654.55 eV correspond to the binding energy of Mn $2p_{3/2}$ and Mn $2p_{1/2}$, respectively. The peaks of C_{PANI}/MnO_2 are centered at 642.25 and 653.95 eV. Both samples have the spin energy separation of 11.70 eV, indicating the presence of MnO_2.[48,49] In addition, the energy separation of 4.8 eV in the Mn 3s spectra (Figure 5d) further

DOI: 10.1021/acsami.5b11955
ACS Appl. Mater. Interfaces 2016, 8, 6040−6050

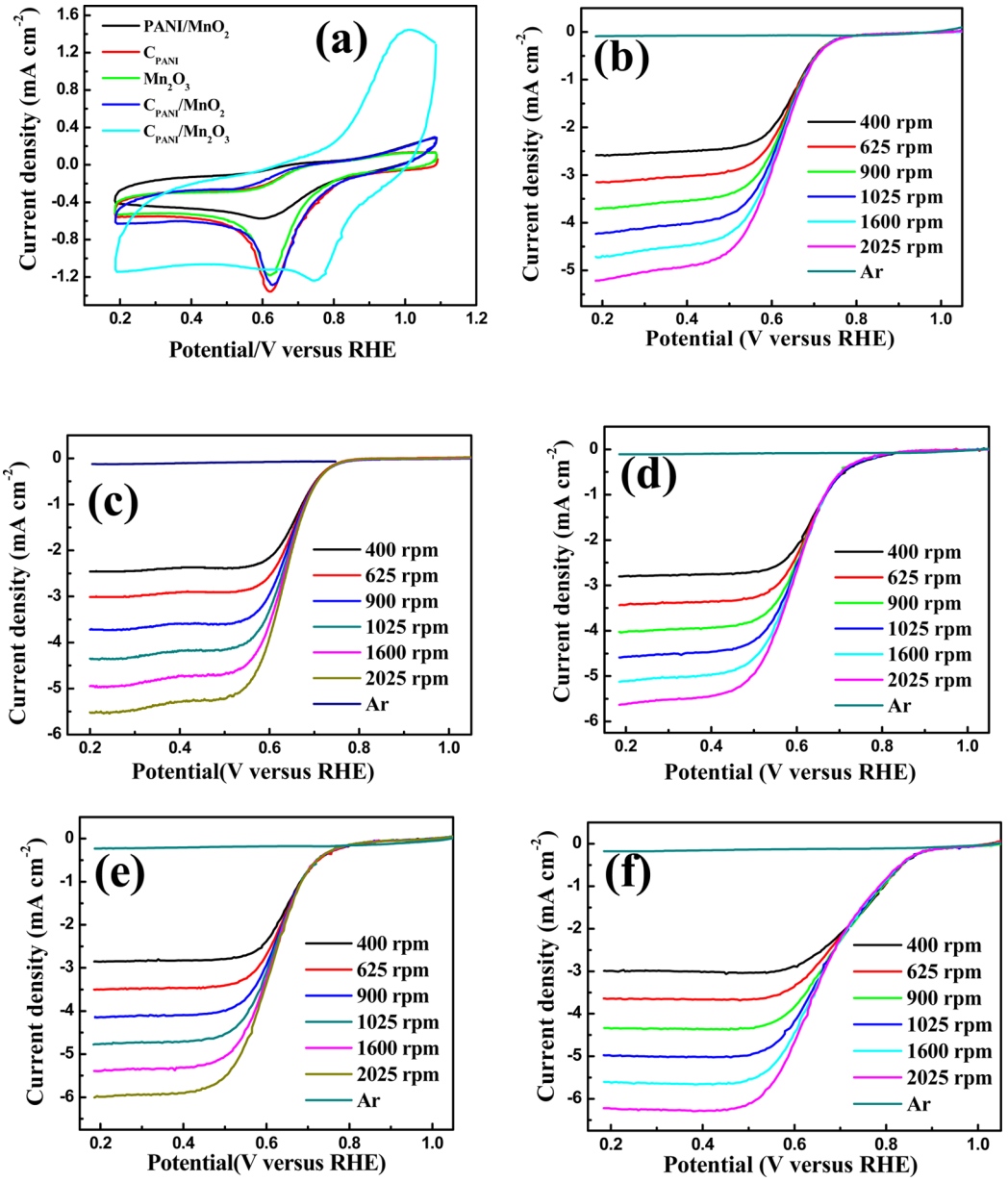

Figure 6. (a) CV profiles of PANI/MnO_2, C_{PANI}, Mn_2O_3, C_{PANI}/MnO_2 and C_{PANI}/Mn_2O_3 supported in GC electrode in O_2-saturated 0.1 mol L^{-1} KOH solution. (b-f) LSV curves of (b) PANI/MnO_2, (c) C_{PANI}, (d) Mn_2O_3, (e) C_{PANI}/MnO_2, and (f) C_{PANI}/Mn_2O_3 samples recorded in Ar- and O_2-saturated 0.1 mol L^{-1} KOH solution at different rotation speed.

indicates MnO_2 to be dominated in the composites.[50] In comparison with PANI/MnO_2 and C_{PANI}/MnO_2, the spin energy separation of 11.78 eV in the Mn 2p spectrum (Figure 5c) and the energy separation of 5.6 eV in the Mn 3s spectrum (Figure 5d) indicates Mn_2O_3 to be dominated in the hybrids.[51,52] Results from XRD, FTIR, Raman and XPS analysis confirm the successful transformation from PANI/MnO_2 to C_{PANI}/MnO_2 and C_{PANI}/Mn_2O_3 hybrid shells through surface protected calcination strategy.

Figure 5e shows the surface area and porosity as measured by N_2 adsorption−desorption isotherms. The measured BET specific surface areas are 55.6, 135.1, 138.1, and 185.3 m^2 g^{-1} for Mn_2O_3, PANI/MnO_2, C_{PANI}/MnO_2, and C_{PANI}/Mn_2O_3 hybrid shells, respectively. Moreover, it should be noted that the surface areas of Mn_2O_3 hollow spheres is minimal comparison with other hollow spheres due to the carbon structure reduction. Figure 5f shows the pore size distribution as determined using the BJH method from the adsorption branch of the isotherm. The average pore diameter of PANI/MnO_2, C_{PANI}/MnO_2, and C_{PANI}/Mn_2O_3 hybrid shells is 4.0 nm; however, Mn_2O_3 hollow spheres has a larger pore size of about 5.0 nm. The results agree well with TEM results (Figures 2a and 3b), where complete removal of carbon in C_{PANI}/Mn_2O_3 hybrid shells leads to increased pore size.

3.2. Electrocatalytic Performance. The ORR performances of different catalysts were then compared. As demonstrated by the cyclic voltammetry (CV) profiles in Figure S5, all the catalytic materials do not show the cathodic reduction peak proving no electrochemical activity in Ar atmosphere. In the case of O_2 atmosphere, the cathodic reduction peaks can be detected for all the catalytic materials. The peak for C_{PANI}/Mn_2O_3 appears at 0.76 V (Figure 6a), significantly higher than that of PANI/MnO_2 (0.61 V), C_{PANI} (0.62 V), C_{PANI}/MnO_2 (0.64 V), and Mn_2O_3 (0.63 V),

DOI: 10.1021/acsami.5b11955
ACS Appl. Mater. Interfaces 2016, 8, 6040−6050

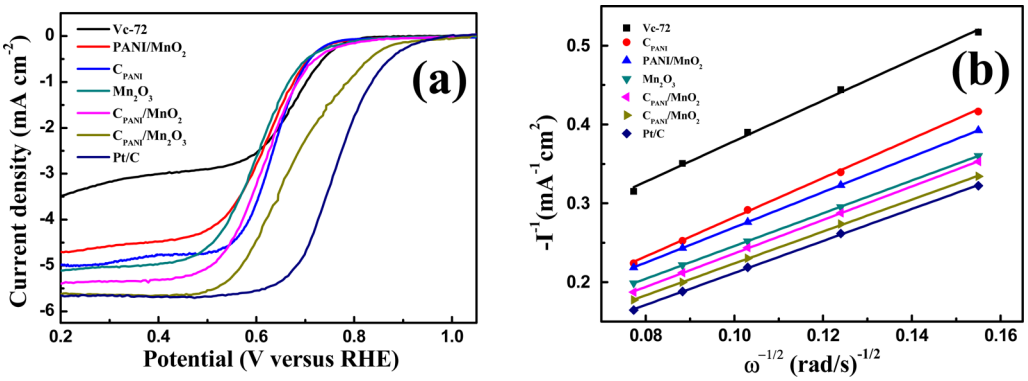

Figure 7. (a) LSV curves of PANI/MnO_2, C_{PANI}, Mn_2O_3, C_{PANI}/MnO_2, C_{PANI}/Mn_2O_3, Vc-72, and Pt/C recorded at 1600 rpm in O_2-saturated 0.1 mol L^{-1} KOH solution. (b) K-L plots of different catalysts at 0.3 V.

revealing that C_{PANI}/Mn_2O_3 hybrid shells have the highest electrocatalytic activity.

RDE measurements were applied to disclose the ORR kinetics. As shown in Figure 6b–f, the linear-sweep voltammetry (LSV) curves of PANI/MnO_2, C_{PANI}, Mn_2O_3, C_{PANI}/MnO_2, and C_{PANI}/Mn_2O_3 at different rotation speeds are given. In Ar-saturated electrolyte, the reduction current is negligible, whereas an obvious increase in reduction current can be observed at O_2 atmosphere. This should be ascribed to the catalytic oxygen reduction. The LSV curves of different samples display a similar shape, and there are two regions of potential–current response: the reduction current increases rapidly from 0.9 to 0.4 V, whereas at potentials below 0.4 V, the reduction current stops increasing and the diffusion-limiting current (i_d) appears. In addition, the reduction current increases with rotation speed due to the increased oxygen flux to the electrode surface.

The LSV curves of different catalysts, Vc-72 and benchmark Pt/C at the same rotation speed (1600 rpm) are shown in Figure 7a. Although the half-wave potential of C_{PANI}/Mn_2O_3 (0.78 V) is lower than that of benchmark Pt/C (0.82 V), it is much higher than that of PANI/MnO_2 (0.71 V), C_{PANI} (0.71 V), C_{PANI}/MnO_2 (0.72 V), and Mn_2O_3 (0.71 V). The i_d of C_{PANI}/Mn_2O_3 (−5.61 mA cm^{-2}) is also higher than that of the other catalysts and is infinitely close to that of benchmark Pt/C (−5.62 mA cm^{-2}, Table 1). Besides, the onset potential is also higher than that of other catalysts (Figure S6 and Table 1). Results confirm that C_{PANI}/Mn_2O_3 hybrid shells show enhanced electrocatalytic activity than PANI/MnO_2, C_{PANI}/MnO_2, and their individual components.

Table 1. Summary of Electrochemical Results for the Synthesized Catalysts and the Benchmark Pt/C[a]

catalyst	E_{onset} (V)	E_{half} (V)	I_s (mA cm^{-2})	I_m (mA mg^{-1})	n
PANI/MnO_2	0.879	0.719	−4.72	55.5	3.59
C_{PANI}	0.861	0.712	−4.98	58.6	3.61
Mn_2O_3	0.852	0.707	−5.12	60.2	3.81
C_{PANI}/MnO_2	0.918	0.722	−5.39	63.4	3.89
C_{PANI}/Mn_2O_3	0.974	0.784	−5.61	66.0	3.84
Pt/C	0.997	0.821	−5.67	66.7	3.95

[a] E_{onset}, E_{half}, I_s, I_m, and n denote onset potential, half-wave potential, specific current, mass current density and electron transfer number, respectively. I_s, I_m, and n correspond to values determined at 0.3 V.

Figure 7b displays the calculated Koutecky–Levich (K–L) plots at a potential of 0.3 V (see Supporting Information for detailed calculation), in which the electron transfer number (n) can be determined from the slope of the fitted linear line. It has been accepted that the ORR on Pt-based and carbonaceous catalysts is dominated by a four-electron and a two-electron transfer mechanism, respectively.[53,54] The lower n value states inferior electrochemical performance. Figure 7b shows that the slope of these samples is close to that of Pt/C especially that of C_{PANI}/Mn_2O_3 and C_{PANI}/MnO_2 (see Table 1 for detailed data), indicating a quasi-four-electron process on these catalysts.

To deeply reveal the ORR pathway, four samples of Mn_2O_3, C_{PANI}/MnO_2, C_{PANI}/Mn_2O_3, and Pt/C with relatively high-efficiency electrocatalytic ORR were further studied using the RRDE. Figure 8a shows the polarization curves recorded on the ring and disk. In comparison with Figure 7a, the voltammetry shape and the catalytic trend on the disk are similar to those with RDE measurement. The intermediate peroxide species produced from the ORR electrocatalysis on the disk can be detected on the ring. The peroxide yield ($y_{peroxide}$) is defined as the percentage of peroxide with respect to the total oxygen reduction products. On account of the disk current (i_d) and ring current (i_r), $y_{peroxide}$ and n can be calculated based on the following equations:

$$y_{peroxide} = 200 i_r/(N i_d + i_r) \quad (1)$$

$$n = 4 N i_d/(N i_d + i_r) \quad (2)$$

where N is the current collection efficiency of RRDE.[54,55] The $y_{peroxide}$ and n values are found to vary with disk potential (Figure 8b). From 0.2 to 0.4 V, the average $y_{peroxide}$ was measured to be ~9.4, ~5.0, and ~5.1 for Mn_2O_3, C_{PANI}/MnO_2, and C_{PANI}/Mn_2O_3, respectively. The corresponding n was 3.81, 3.89, and 3.84, respectively. Close to Pt/C, the ORR catalyzed by Mn_2O_3, C_{PANI}/MnO_2, and C_{PANI}/Mn_2O_3 was mainly through a quasi-four-electron transfer process. The results are consistent with those from the K–L determination (Figure S7). Thus, the RRDE data confirm that Mn_2O_3, C_{PANI}/MnO_2 and C_{PANI}/Mn_2O_3 exhibited remarkable catalytic activities.

In addition, their high activity can also be determined by the Tafel curves (Figure 9), in which the kinetic current (i_k) is originated from the mass-transport correction ($i_k = (i \times i_d)/(i_d - i)$).[56] At low and high overpotentials, two linear regions can be seen, where the slopes are close to −2.303RT/F (−59 mV dec^{-1}) and −2.303(2RT/F) (−118 mV dec^{-1}) with temperature set at 25 °C, respectively. C_{PANI}/Mn_2O_3 hybrid shells with

DOI: 10.1021/acsami.5b11955
ACS Appl. Mater. Interfaces 2016, 8, 6040–6050

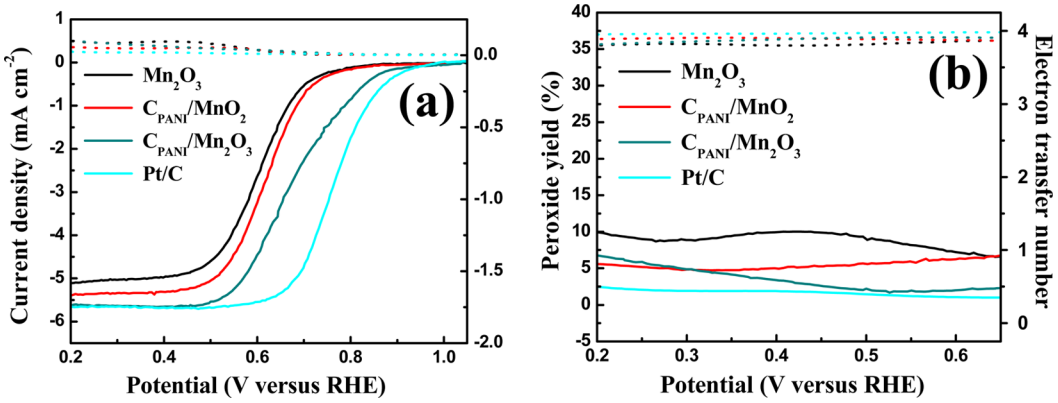

Figure 8. (a) The polarization curves of Mn_2O_3, C_{PANI}/MnO_2, C_{PANI}/Mn_2O_3 and Pt/C recorded on disk (solid line) and the ring (dotted line). (b) Peroxide yield (solid line) and the electron transfer number (dotted line) of Mn_2O_3, C_{PANI}/MnO_2, C_{PANI}/Mn_2O_3, and Pt/C at different potentials.

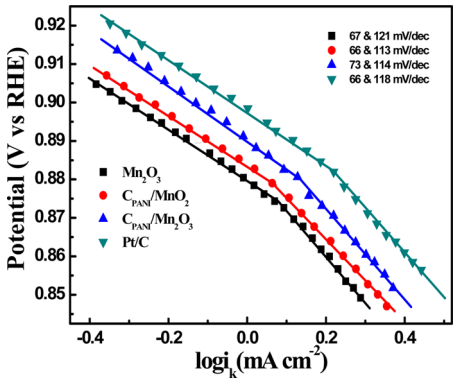

Figure 9. Tafel plots of Mn_2O_3, C_{PANI}/MnO_2, C_{PANI}/Mn_2O_3, and Pt/C derived by the mass-transport correction of corresponding LSV data under 1600 rpm.

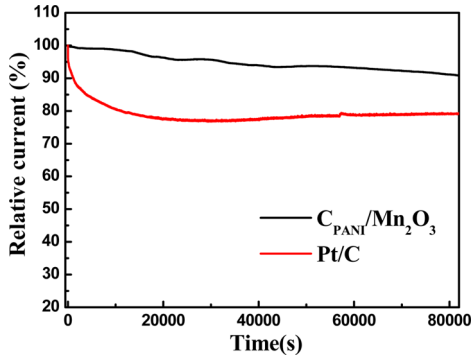

Figure 10. Chronoamperometric curves (percentage of retained current as a function of operation time) of C_{PANI}/Mn_2O_3 and Pt/C electrodes maintained at 0.8 V versus RHE in O_2-saturated 0.1 M KOH electrolyte.

slops of 73 mV dec^{-1} and 114 mV dec^{-1} are close to those of Pt/C (66 mV dec^{-1} and 118 mV dec^{-1}). This feature is consistent with previously reported manganese oxide electrocatalysts, where the rate-determining step at catalyst surface is believed to be the first electron reduction of oxygen.[54,57] In addition, other samples with two similar Tafel slopes also indicate a similar reaction mechanism. On transition metal oxides of alkaline media, the ORR electrocatalysis mechanism is normally suggested to involve the following steps: O_2 adsorption, formation of HO_2^-, and further reduction or decomposition of peroxide to OH^-.[58] All the steps are strongly dependent on the catalyst surface oxygen adsorption ability and number of available active sites and mediated by electron transfer and redox reactions of metal-containing species.[54,59] Like this reaction mechanism, the intermediate HO_2^- first formed on catalyst surfaces, and the redox between Mn species and the introduction of carbon are convinced to favor the charge transfer involved in oxygen reduction.[60,61]

The catalytic stability of C_{PANI}/Mn_2O_3 hybrid shells was also investigated (Figure 10). In a continuous polarization period (22.2 h), the chronoamperometric ORR current retention for C_{PANI}/Mn_2O_3 hybrid shells is 91.1%, significantly higher than that of the counterpart Pt/C (79.4%). In addition, the electrocatalysts of C_{PANI}/Mn_2O_3 hybrid shells still keep the original hollow morphology (Figure S9). Results confirm considerable catalytic stability of C_{PANI}/Mn_2O_3 hybrid shells involved in ORR electrocatalysis.

Table 1 summarizes the ORR electrocatalytic characteristics of the composites. All the results indicated mesoporous C_{PANI}/Mn_2O_3 hybrid shells exhibit the best overall oxygen reduction activity. Furthermore, the mesoporous C_{PANI}/Mn_2O_3 hybrid shells also show superior performances involved in ORR than reported Mn_xO_y and/or carbon-based materials (Table S1). The high ORR catalytic activity should be ascribed to the following factors: high specific surface area, crystal structure of the Mn−O material, and complex with N-doped carbon. At first, C_{PANI}/Mn_2O_3 hybrids possess high specific surface area (185.3 m^2 g^{-1}) and mesoporous shells (average pore diameter of 4.0 nm), which enhance the oxygen adsorption and made the oxygen get electrons easier during the redox reaction. Second, in alkaline media, mesoporous Mn_2O_3 is excellent in intrinsic because of its unique crystal structure.[62] The oxidation state of Mn exists in Mn^{3+} cations, and the presence of 3d metals will benefit electron conduction (by hopping) and charge transfer (through redox reactions), thus favoring the electrocatalysis.[63] Finally, the introduction of N-doped carbon obtained by carbonized PANI not only contributes to active sites but also enhances the electron transfer process. The Nyquist plot of C_{PANI}/Mn_2O_3 hybrid shells shows the smallest semicircle in the middle-frequency region, followed by Mn_2O_3 and C_{PANI} (Figure S8). Result indicates the reduced electron transfer resistance after the introduction of C_{PANI}, and thus promotes the catalytic activity of the hybrids.[35,36,64] Therefore, mesoporous C_{PANI}/Mn_2O_3 hybrid shells show high performance

DOI: 10.1021/acsami.5b11955
ACS Appl. Mater. Interfaces 2016, 8, 6040−6050

catalysts because of its structure and composition codependent behavior.

4. CONCLUSION

Mesoporous hybrid shells of C_{PANI}/Mn_2O_3 have been synthesized through surface protected calcination processes and their electrocatalytic activities toward ORR have been revealed. Compared with PANI/MnO_2 and C_{PANI}/MnO_2 hybrid shells and their individual components of Mn_2O_3 and C_{PANI}, C_{PANI}/Mn_2O_3 hybrid shells exhibit the highest electrocatalytic activities toward ORR with their current density and electron transfer number comparable to those of the benchmark Pt/C. Catalytic properties of C_{PANI}/Mn_2O_3 hybrid shells have been found to be closely related to their high specific surface area, the surface oxidation state of Mn and composition codependent behavior. This study not only supplies an elegantly controlled route for hollow-structured mesoporous hybrids of holey carbon and metal oxide but also, more importantly, provides an effective strategy to prepare cheap, high-performance nonprecious electrocatalysts for ORR.

■ ASSOCIATED CONTENT

Supporting Information

The Supporting Information is available free of charge on the ACS Publications website at DOI: 10.1021/acsami.5b11955.

Additional structure and electrochemical characterization. (PDF)

■ AUTHOR INFORMATION

Corresponding Authors

*E-mail: hanjie@yzu.edu.cn.
*E-mail: guorong@yzu.edu.cn.

Notes

The authors declare no competing financial interest.

■ ACKNOWLEDGMENTS

The authors gratefully acknowledge financial support from the National Natural Science Foundation of China (No. 21273004), and the Priority Academic Program Development of Jiangsu Higher Education Institutions. We would also like to acknowledge the technical support received at the Testing Center of Yangzhou University.

■ REFERENCES

(1) Steele, B. C. H.; Heinzel, A. Materials for Fuel-Cell Technologies. *Nature* **2001**, *414*, 345−352.
(2) Malavasi, L.; Fisher, C. A. J.; Islam, M. S. Testing the Chemical/Structural Stability of Proton Conducting Perovskite Ceramic Membranes by In Situ/Ex Situ Autoclave Raman Microscopy. *Chem. Soc. Rev.* **2010**, *39*, 4370−4387.
(3) Christensen, P. A.; Hamnett, A.; Linares-Moya, D. Nitrogen-Doped Graphene Nanosheets as High Efficient Catalysts for Oxygen Reduction Reaction. *Phys. Chem. Chem. Phys.* **2011**, *13*, 5206−5214.
(4) Bruce, P. G.; Freunberger, S. A.; Hardwick, L. J.; Tarascon, J. M. Challenges Facing Lithium Batteries. *Nat. Mater.* **2012**, *11*, 19−29.
(5) Stamenkovic, V. R.; Fowler, B.; Mun, B. S.; Wang, G.; Ross, P. N.; Lucas, C. A.; Markovic, N. M. Improved Oxygen Reduction Activity on Pt3Ni(111) Via Increased Surface Site Availability. *Science* **2007**, *315*, 493−497.
(6) Komanicky, V.; Iddir, H.; Chang, K. C.; Menzel, A.; Karapetrov, G.; Hennessy, D.; Zapol, P.; You, H. Shape-Dependent Activity of Platinum Array Catalyst. *J. Am. Chem. Soc.* **2009**, *131*, 5732−5733.
(7) Qian, Y.; Wen, W.; Adcock, P. A.; Jiang, Z.; Hakim, N.; Saha, M. S.; Mukerjee, S. PtM/C Catalyst Prepared Using Reverse Micelle Method for Oxygen Reduction Reaction in PEM Fuel Cells. *J. Phys. Chem. C* **2008**, *112*, 1146−1157.
(8) Zhang, G. Q.; Xia, B. Y.; Wang, X.; Lou, X. W. Strongly Coupled $NiCo_2O_4$-rGO Hybrid Nanosheets as a Methanol-Tolerant Electrocatalyst for the Oxygen Reduction Reaction. *Adv. Mater.* **2014**, *26*, 2408−2412.
(9) Feng, Y. J.; Alonso-Vante, N. Non-Precious Metal Catalysts for the Molecular Oxygen Reduction Reaction. *Phys. Status Solidi B* **2008**, *245*, 1792−1806.
(10) Chen, Z. W.; Higgins, D.; Yu, A.; Zhang, L.; Zhang, J. J. A Review on Non-Precious Metal Electrocatalysts for PEM Fuel Cells. *Energy Environ. Sci.* **2011**, *4*, 3167−3192.
(11) Cao, R.; Lee, J. S.; Liu, M.; Cho, J. Recent Progress in Non-Precious Catalysts for Metal-Air Batteries. *Adv. Energy Mater.* **2012**, *2*, 816−829.
(12) Cheng, F.; Chen, J. Metal-Air Batteries: From Oxygen Reduction Electrochemistry to Cathode Catalysts. *Chem. Soc. Rev.* **2012**, *41*, 2172−2192.
(13) Wang, B. J. Recent Development of Non-Platinum Catalysts for Oxygen Reduction Reaction. *J. Power Sources* **2005**, *152*, 1−15.
(14) Anson, F. C.; Shi, C.; Steiger, B. Novel Multinuclear Catalysts for the Electroreduction of Dioxygen Directly to Water. *Acc. Chem. Res.* **1997**, *30*, 437−444.
(15) Feng, Y.; He, T.; Alonso-Vante, N. In Situ Free-Surfactant Synthesis and ORR-Electrochemistry of Carbon-Supported Co_3S_4 and $CoSe_2$ Nanoparticles. *Chem. Mater.* **2008**, *20*, 26−28.
(16) Xiao, W.; Wang, D.; Lou, X. W. Shape-Controlled Synthesis of MnO_2 Nanostructures with Enhanced Electrocatalytic Activity for Oxygen Reduction. *J. Phys. Chem. C* **2010**, *114*, 1694−1700.
(17) Li, L.; Feng, X. H.; Nie, Y.; Chen, S.; Shi, F.; Xiong, K.; Ding, W.; Qi, X. Q.; Hu, J. S.; Wei, Z. D.; Wan, L. J.; Xia, M. R. Insight into the Effect of Oxygen Vacancy Concentration on the Catalytic Performance of MnO_2. *ACS Catal.* **2015**, *5*, 4825−4832.
(18) Tang, Q. W.; Jiang, L. H.; Liu, J.; Wang, S. L.; Sun, G. Q. Effect of Surface Manganese Valence of Manganese Oxides on the Activity of the Oxygen Reduction Reaction in Alkaline Media. *ACS Catal.* **2014**, *4*, 457−463.
(19) Gong, K.; Yu, P.; Su, L.; Xiong, S.; Mao, L. Polymer-Assisted Synthesis of Manganese Dioxide/Carbon Nanotube Nanocomposite with Excellent Electrocatalytic Activity Toward Reduction of Oxygen. *J. Phys. Chem. C* **2007**, *111*, 1882−1887.
(20) Cheng, F. Y.; Shen, J.; Ji, W. Q.; Tao, Z. L.; Chen, J. Selective Synthesis of Manganese Oxide Nanostructures for Electrocatalytic Oxygen Reduction. *ACS Appl. Mater. Interfaces* **2009**, *1*, 460−466.
(21) Cheng, F. Y.; Su, Y.; Liang, J.; Tao, Z. L.; Chen, J. MnO_2-Based Nanostructures as Catalysts for Electrochemical Oxygen Reduction in Alkaline Media. *Chem. Mater.* **2010**, *22*, 898−905.
(22) Mao, L.; Zhang, D.; Sotomura, T.; Nakatsu, K.; Koshiba, N.; Ohsaka, T. Mechanistic Study of the Reduction of Oxygen in Air Electrode with Manganese Oxides as Electrocatalysts. *Electrochim. Acta* **2003**, *48*, 1015−1021.
(23) Cao, Y. L.; Yang, H. X.; Ai, X. P.; Xiao, L. F. The Mechanism of Oxygen Reduction on MnO_2-Catalyzed Air Cathode in Alkaline Solution. *J. Electroanal. Chem.* **2003**, *557*, 127−134.
(24) Verma, A.; Jha, A. K.; Basu, S. Manganese Dioxide as A Cathode Catalyst for A Direct Alcohol or Sodium Borohydride Fuel Cell with A Flowing Alkaline Electrolyte. *J. Power Sources* **2005**, *141*, 30−34.
(25) Yang, J.; Xu, J. J. Nanostructured Amorphous Manganese Oxide Cryogel as a High-Rate Lithium Intercalation Host. *Electrochem. Commun.* **2003**, *5*, 306−311.
(26) Martin, E.; Tartakovsky, B.; Savadogo, O. Cathode Materials Evaluation in Microbial Fuel Cells: A Comparison of Carbon, Mn_2O_3, Fe_2O_3 and Platinum Materials. *Electrochim. Acta* **2011**, *58*, 58−66.
(27) Tan, Y.; Xu, C.; Chen, G.; Fang, X.; Zheng, N.; Xie, Q. Facile Synthesis of Manganese-Oxide-Containing Mesoporous Nitrogen-Doped Carbon for Efficient Oxygen Reduction. *Adv. Funct. Mater.* **2012**, *22*, 4584−4591.

DOI: 10.1021/acsami.5b11955
ACS Appl. Mater. Interfaces 2016, 8, 6040−6050

(28) Guo, J.; Liu, Q.; Wang, C.; Zachariah, M. R. Interdispersed Amorphous MnO_x-Carbon Nanocomposites with Superior Electrochemical Performance as Lithium-Storage Material. *Adv. Funct. Mater.* **2012**, *22*, 803−811.
(29) Chandra, S.; Das, P.; Bag, S.; Bhar, R.; Pramanik, P. Mn_2O_3 Decorated Graphene Nanosheet: An Advanced Material for The Photocatalytic Degradation of Organic Dyes. *Mater. Sci. Eng., B* **2012**, *177*, 855−861.
(30) Wang, X.; Liu, L.; Wang, X.; Yi, L.; Hu, C.; Zhang, X. Mn_2O_3/Carbon Aerogel Microbead Composites Synthesized by In Situ Coating Method for Supercapacitors. *Mater. Sci. Eng., B* **2011**, *176*, 1232−1238.
(31) Park, K. W. Carboxylated Graphene Oxide-Mn_2O_3 Nanorod Composites for Their Electrochemical Characteristics. *J. Mater. Chem. A* **2014**, *2*, 4292−4298.
(32) Jasinski, R. A New Fuel Cell Cathode Catalyst. *Nature* **1964**, *201*, 1212−1213.
(33) Gupta, S.; Tryk, D.; Bae, I.; Aldred, W.; Yeager, E. Heat-Treated Polyacrylonitrile-Based Catalysts for Oxygen Electroreduction. *J. Appl. Electrochem.* **1989**, *19*, 19−27.
(34) (a) Wu, G.; More, K. L.; Johnston, C. M.; Zelenay, P. High-Performance Electrocatalysts for Oxygen Reduction Derived From Polyaniline, Iron, and Cobalt. *Science* **2011**, *332*, 443−447. (b) Ding, W.; Wei, Z. D.; Chen, S. G.; Qi, X. Q.; Yang, T.; Hu, J. S.; Wang, D.; Wan, L. J.; Alvi, S. F.; Li, L. Space-Confinement-Induced Synthesis of Pyridinic- and Pyrrolic-Nitrogen-Doped Graphene for the Catalysis of Oxygen Reduction. *Angew. Chem., Int. Ed.* **2013**, *52*, 11755−11759.
(35) (a) Silva, R.; Voiry, D.; Chhowalla, M.; Asefa, T. Efficient Metal-Free Electrocatalysts for Oxygen Reduction: Polyaniline-Derived N- and O-doped Mesoporous Carbons. *J. Am. Chem. Soc.* **2013**, *135*, 7823−7826. (b) Ding, W.; Li, L.; Xiong, K.; Wang, Y.; Li, W.; Nie, Y.; Chen, S. G.; Qi, X. Q.; Wei, Z. D. Shape Fixing Via Salt Recrystallization: A Morphology-Controlled Approach to Convert Nanostructured Polymer to Carbon Nanomaterial as A Highly Active Catalyst for Oxygen Reduction Reaction. *J. Am. Chem. Soc.* **2015**, *137*, 5414−5420.
(36) Wu, R.; Chen, S. G.; Zhang, Y. L.; Wang, Y.; Ding, W.; Li, L.; Qi, X. Q.; Shen, X.; Wei, Z. D. Template-Free Synthesis of Hollow Nitrogen-Doped Carbon as Efficient Electrocatalysts for Oxygen Reduction Reaction. *J. Power Sources* **2015**, *274*, 645−650.
(37) Han, J.; Li, L.; Fang, P.; Guo, R. Ultrathin MnO_2 Nanorods on Conducting Polymer Nanofibers as A New Class of Hierarchical Nanostructures for High-Performance Supercapacitors. *J. Phys. Chem. C* **2012**, *116*, 15900−15907.
(38) Liu, R.; Duay, J.; Lee, S. B. Redox Exchange Induced MnO_2 Nanoparticle Enrichment in Poly(3,4-Ethylenedioxythiophene) Nanowires for Electrochemical Energy Storage. *ACS Nano* **2010**, *4*, 4299−4307.
(39) Wong, Y. J.; Zhu, L.; Teo, W. S.; Tan, Y. W.; Yang, Y.; Wang, C.; Chen, H. Revisiting The Stöber Method: in Homogeneity in Silica Shells. *J. Am. Chem. Soc.* **2011**, *133*, 11422−11425.
(40) Han, J.; Li, L.; Guo, R. Novel Approach to Controllable Synthesis of Gold Nanoparticles Supported on Polyaniline Nanofibers. *Macromolecules* **2010**, *43*, 10636−10644.
(41) Ping, Z. In Situ FTIR-Attenuated Total Reflection Spectroscopic Investigations on The Base−Acid Transitions of Polyaniline. Base−Acid Transition in the Emeraldine Form of Polyaniline. *J. Chem. Soc., Faraday Trans.* **1996**, *92*, 3063−3067.
(42) Furukawa, Y.; Ueda, F.; Hyodo, Y.; Harada, I.; Nakajima, T.; Kawagoe, T. Vibrational Spectra and Structure of Polyaniline. *Macromolecules* **1988**, *21*, 1297−1305.
(43) Šeděnková, I.; Trchová, M.; Blinova, N. V.; Stejskal, J. In-Situ Polymerized Polyaniline Films: Preparation in Solutions of Hydrochloric, Sulfuric, or Phosphoric Acid. *Thin Solid Films* **2006**, *515*, 1640−1646.
(44) Mentus, S.; Ciric-Marjanovic, G.; Trchova, M.; Stejskal, J. Conducting Carbonized Polyaniline Nanotubes. *Nanotechnology* **2009**, *20*, 245601.
(45) Dresselhaus, M. S.; Jorio, A.; Hofmann, M.; Dresselhaus, G.; Saito, R. Perspectives on Carbon Nanotubes and Graphene Raman Spectroscopy. *Nano Lett.* **2010**, *10*, 751−758.
(46) Gholap, S.; Badiger, M.; Gopinath, C. S. Molecular Origins of Wettability of Hydrophobic Poly(vinylidene fluoride) Microporous Membranes on Poly(vinyl alcohol) Adsorption: Surface and Interface Analysis by XPS. *J. Phys. Chem. B* **2005**, *109*, 13941−13947.
(47) Toupin, M.; Brousse, T.; Bélanger, D. Influence of Microstucture on the Charge Storage Properties of Chemically Synthesized Manganese Dioxide. *Chem. Mater.* **2002**, *14*, 3946−3952.
(48) Wang, L. C.; Liu, Y. M.; Chen, M.; Cao, Y.; He, H. Y.; Fan, K. N. MnO_2 Nanorod Supported Gold Nanoparticles with Enhanced Activity for Solvent-Free Aerobic Alcohol Oxidation. *J. Phys. Chem. C* **2008**, *112*, 6981−6987.
(49) Hou, Y.; Cheng, Y.; Hobson, T.; Liu, J. Design and Synthesis of Hierarchical MnO_2 Nanospheres/Carbon Nanotubes/Conducting Polymer Ternary Composite for High Performance Electrochemical Electrodes. *Nano Lett.* **2010**, *10*, 2727−2733.
(50) Murugan, B.; Ramaswamy, A. V.; Srinivas, D.; Gopinath, C. S.; Ramaswamy, V. Nature of Manganese Species in $Ce_{1-x}Mn_xO_{2-\delta}$ Solid Solutions Synthesized by The Solution Combustion Route. *Chem. Mater.* **2005**, *17*, 3983−3993.
(51) Han, Y. F.; Chen, L. W.; Ramesh, K.; Zhong, Z. Y.; Chen, F.; Chin, J.; Mook, H. Coral-liken Anostructured Alpha-Mn_2O_3 Nanaocrystals for Catalytic Combustion of Methane - Part I. Preparation and Characterization. *Catal. Today* **2008**, *131*, 35−41.
(52) Christensen, P. A.; Hamnett, A.; Linares-Moya, D. Oxygen Reduction and Fuel Oxidation in Alkaline Solution. *Phys. Chem. Chem. Phys.* **2011**, *13*, 5206−5214.
(53) Cheng, F. Y.; Chen, J. Metal-Air Batteries: From Oxygen Reduction Electrochemistry to Cathode Catalysts. *Chem. Soc. Rev.* **2012**, *41*, 2172−2192.
(54) Roche, I.; Chainet, E.; Chatenet, M.; Vondrák, J. Carbon-Supported Manganese Oxide Nanoparticles as Electrocatalysts for the Oxygen Reduction Reaction (ORR) in Alkaline Medium: Physical Characterizations and ORR Mechanism. *J. Phys. Chem. C* **2007**, *111*, 1434−1443.
(55) Liang, Y.; Wang, H.; Zhou, J.; Li, Y.; Wang, J.; Regier, T.; Dai, H. J. Covalent Hybrid of Spinel Manganese-Cobalt Oxide and Graphene as Advanced Oxygen Reduction Electrocatalysts. *J. Am. Chem. Soc.* **2012**, *134*, 3517−3523.
(56) Han, X.; Zhang, T.; Du, J.; Cheng, F.; Chen, J. Porous Calcium−Manganese Oxide Microspheres for Electrocatalytic Oxygen Reduction with High Activity. *Chem. Sci.* **2013**, *4*, 368−376.
(57) Rios, E.; Abarca, S.; Daccarett, P.; Nguyen Cong, H.; Martel, D.; Marco, J. F.; Gancedo, J. R.; Gautier, J. L. Electrocatalysis of Oxygen Reduction on Cu(x)Mn(3-x)O(4) ($1.0 \leq x \leq 1.4$) Spinel Particles/Polypyrrole Composite Electrodes. *Int. J. Hydrogen Energy* **2008**, *33*, 4954−4954.
(58) Suntivich, J.; Gasteiger, H. A.; Yabuuchi, N.; Nakanishi, H.; Goodenough, J. B.; Shao-Horn, Y. Design Principles for Oxygen-Reduction Activity on Perovskite Oxide Catalysts for Fuel Cells and Metal-Air Batteries. *Nat. Chem.* **2011**, *3*, 546−550.
(59) Oh, S. H.; Black, R.; Pomerantseva, E.; Lee, J. H.; Nazar, L. F. Synthesis of a Metallic Mesoporous Pyrochlore as a Catalyst for Lithium-O_2 Batteries. *Nat. Chem.* **2012**, *4*, 1004−1010.
(60) (a) Lima, F. H. B.; Calegaro, M. L.; Ticianelli, E. A. Investigations of the Catalytic Properties of Manganese Oxides for The Oygen Reduction Reaction in Alkaline Media. *J. Electroanal. Chem.* **2006**, *590*, 152−160. (b) Lima, F. H. B.; Calegaro, M. L.; Ticianelli, E. A. Electrocatalytic Activity of Manganese Oxides Prepared by Thermal Decomposition for Oxygen Reduction. *Electrochim. Acta* **2007**, *52*, 3732−3738.
(61) (a) Gong, K.; Yu, P.; Su, L.; Xiong, S.; Mao, L. Polymer-Assisted Synthesis of Manganese Dioxide/Carbon Nanotube Nanocomposite with Excellent Electrocatalytic Activity Toward Reduction of Oxygen. *J. Phys. Chem. C* **2007**, *111*, 1882−1887. (b) Mao, L.; Zhang, D.; Sotomura, T.; Nakatsu, K.; Koshiba, N.; Ohsaka, T. Mechanistic Study of The Reduction of Oxygen in Air Electrode with Manganese Oxides

DOI: 10.1021/acsami.5b11955
ACS Appl. Mater. Interfaces 2016, 8, 6040−6050

as Electrocatalysts. *Electrochim. Acta* **2003**, *48*, 1015−1021. (c) Mao, L.; Sotomura, T.; Nakatsu, K.; Koshiba, N.; Zhang, D.; Ohsaka, T. Electrochemical Characterization of Catalytic Activities of Manganese Oxides to Oxygen Reduction in Alkaline Aqueous Aolution. *J. Electrochem. Soc.* **2002**, *149*, A504−A507.

(62) Dong, H. Q.; Chen, Y. Y.; Han, M.; Li, S. L.; Zhang, J.; Li, J. S.; Lan, Y. Q.; Dai, Z. H.; Bao, J. C. Synergistic Effect of Mesoporous Mn_2O_3-Supported Pd Nanoparticle Catalysts for Eelectrocatalytic Oxygen Reduction Reaction with Enhanced Performance in Alkaline Medium. *J. Mater. Chem. A* **2014**, *2*, 1272−1276.

(63) Cheng, F. Y.; Zhang, T. R.; Zhang, Y.; Du, J.; Han, X. P.; Chen, J. Enhancing Electrocatalytic Oxygen Reduction on MnO_2 with Vacancies. *Angew. Chem., Int. Ed.* **2013**, *52*, 2474−2477.

(64) (a) Kitaura, R.; Imazu, N.; Kobayashi, K.; Shinohara, H. Fabrication of Metal Nanowires in Carbon Nanotubes via Versatile Nano-Template Reaction. *Nano Lett.* **2008**, *8*, 693−699. (b) Guo, S.; Dong, S. Graphene Nanosheet: Synthesis, Molecular Engineering, Thin Film, Hybrids, and Energy and Analytical Applications. *Chem. Soc. Rev.* **2011**, *40*, 2644−2672.

DOI: 10.1021/acsami.5b11955
ACS Appl. Mater. Interfaces 2016, 8, 6040−6050